Ganymede–induced decametric radio emission: in-situ observations and measurements by Juno

C. K. Louis[1], P. Louarn[1], F. Allegrini[2,3], W. S. Kurth [4], J. R. Szalay[5]

[1]IRAP, Universit de Toulouse, CNRS, CNES, UPS, (Toulouse), France
[2]Southwest Research Institute, San Antonio, Texas, USA
[3]Department of Physics and Astronomy, University of Texas at San Antonio, San Antonio, Texas, USA
[4]Department of Physics and Astronomy, University of Iowa, Iowa City, Iowa, USA
[5]Department of Astrophysical Sciences, Princeton University, Princeton, New Jersey, USA

Key Points:

- First detailed wave/particle investigation of a Ganymede-induced decametric radio source using Juno/Waves and Juno/JADE instruments
- Confirmation that the emission is produced by a loss-cone-driven Cyclotron Maser Instability
- Ganymede-induced radio emission is produced by electrons of $\sim$ 4-15 keV, at a beaming angle [76°-83°], and a frequency $1.005 - 1.021 \times f_{ce}$

Corresponding author: C. K. Louis, `corentin.louis@irap.omp.eu`

Abstract

At Jupiter, part of the auroral radio emissions are induced by the Galilean moons Io, Europa and Ganymede. Until now, they have been remotely detected, using ground-based radio-telescopes or electric antennas aboard spacecraft. The polar trajectory of the Juno orbiter allows the spacecraft to cross the magnetic flux tubes connected to these moons, or their tail, and gives a direct measure of the characteristics of these decametric moon–induced radio emissions. In this study, we focus on the detection of a radio emission during the crossing of the Ganymede flux tube. Using electromagnetic waves (Juno/Waves) and in-situ electron measurements (Juno/JADE-E), we estimate the flux tube width to be a few 100 km, a growth rate of the radio emission $> 3 \times 10^{-4}$, an electron population of energy $E = 4 - 15$ keV and an emission beaming angle of $\theta = 76° - 83°$, at a frequency $\sim 1.005 - 1.021 \times f_{ce}$. We also confirmed that radio emission is associated with Ganymede's down-tail far-ultraviolet emission.

Plain Language Summary

The Juno spacecraft crossed magnetic field lines connected to Ganymede's auroral signature in Jupiter's atmosphere. At the same time, Juno also crossed a decametric radio source. By measuring the electrons during this radio source crossing, we determine that this emission is produced by the cyclotron maser instability driven by upgoing electrons, at a frequency 0.5 to 2.1% above the cyclotron electronic frequency with electrons of energy 4-15 keV.

1 Introduction

With the arrival of Juno at Jupiter in July 2016, the probe passes above the poles once per orbit, every 53 days, and acquires high-resolution measurements in the auroral regions (Bagenal et al., 2017). In particular the Waves (radio and plasma waves instrument, Kurth et al., 2017), JADE (Jovian Auroral Distributions Experiment, McComas et al., 2017, providing electron measurements) and MAG (Magnetometer experiment, Connerney et al., 2017) instruments offer a unique opportunity to investigate in-situ the Jovian radio emissions produced in these polar regions. These instruments enable constraints on the position of the sources (Louis et al., 2019; Imai et al., 2017, 2019) and the mechanism producing these emissions (Louarn et al., 2017, 2018), the Cyclotron Maser Instability (CMI) which is also responsible for the production of the auroral kilometric radiation at Earth and Saturn (Treumann, 2006; Wu, 1985; Wu & Lee, 1979; Le Queau et al., 1984b, 1984a; Pritchett, 1986a).

This instability produces emissions very close to the electron cyclotron frequency f_{ce}, and requires two primary conditions : (i) a magnetized plasma, where the electron plasma frequency f_{pe} (proportional to the square root of the electron plasma density n_e) is much lower than the electron cyclotron frequency f_{ce} (proportional to the magnetic field amplitude B); and (ii) a weakly relativistic electron population previously accelerated along high-latitude magnetic field lines at typical energies of a few keV. The first orbits of Jupiter allowed Louarn et al. (2017, 2018) to study in-situ the radio emission during source crossings and determine that the auroral hectometric/decametric radio emissions are driven by the CMI with a loss cone distribution function, i.e. triggered by a lack in the up-going electron population.

The Jupiter auroral radio emission is split into three major components, depending on the emission wavelength, namely broadband kilometric, hectometric and decametric. Part of the auroral radio emissions in the decametric range are induced by the interaction between the jovian magnetosphere and the following Galilean moons: the best known case Io, discovered by Bigg (1964), and Europa and Ganymede (Louis, Lamy, Zarka, Cecconi, & Hess, 2017; Zarka et al., 2018, 2017). These three moons are also known to

induce Far Ultraviolet (FUV) aurora above Jupiter's atmosphere (Prangé et al., 1996; Clarke, 1998; Clarke et al., 2002).

In the Io case, we know that FUV and radio auroral emission are produced by Alfvnic interactions, and that Io-induced radio emissions are produced on the magnetic field lines connected to the main Alfvn wing (MAW) and reflected Alfvn wing (RAW) spots (Hess et al., 2010). In the Europa and Ganymede case, no simultaneous observation of FUV and radio emissions has yet been obtained.

In this study, we focus on Juno's crossing of field lines connected to Ganymede's footprint tail, which took place on May 29, 2019, where simultaneous FUV (Szalay et al., 2020a) and radio emission were observed (see Section 2). In Section 3 we present the instability leading to radio emission and the calculation to determine the different parameters of the radio emission (growth rate, electron distribution function and energy, opening of the emission cone). Finally in Section 4 we summarize and discuss the results.

2 Observations

On May 29^{th}, 2019 between 07:37:14 and 07:37:32, Juno crossed the magnetic field tube connected to Ganymede's tail ($\sim 8°$ downtail from Ganymede's main auroral spot). The in-situ measurements of Juno/MAG and Juno/JADE for the down-going electrons and the Juno/UVS images were used by Szalay et al. (2020a) to show the presence of Alfvn wave activity capable of accelerating electrons into the atmosphere and producing FUV emissions, observed at the footprint of the crossed magnetic field lines. Here we focus on the study of Juno/JADE for the up-going electrons and the radio measurements of Juno/Waves.

Figure 1 displays Juno measurements around the Ganymede flux tube encounter. Panel (a) presents the Juno/Waves measurements (low resolution mode) around the twentieth perijove ($\sim -2/+1$ h). Panel (b) is a 5-minute zoom-in of panel (a) using the Juno/Waves high-resolution mode. The solid-white line represents $f_{\rm ce}$ while the dashed-white line (panel b) represents $1.01\times f_{\rm ce}$ (typical frequency for a loss-cone-CMI-driven emission with electron energy of ~ 5 keV, see Louarn et al., 2017). Panels (c–f) display Juno/JADE-E (electrons) measurements, with panel (c) presenting the electron differential energy flux, panels (d-e) the electron distribution functions for energy in range [2-21] keV for different pitch angle ranges (panel (e) showing a subset for pitch angle corresponding to up-going electrons) and panel (f) the partial electron density (all the low energy population (here < 0.050 keV) is not accounted for).

Figure 1b displays an emission very close to $f_{\rm ce}$, tangent to the $1.01\times f_{ce}$ line, between $\sim$ 07:37:00 and $\sim$ 07:38:10. During this time interval, and more precisely between $\sim$ 07:37:14 and ~07:37:32 (during Ganymede's tail crossing), we observe an enhancement in the electron energy flux (panel c) at a few keV, strong intensification in the distribution function (panel d) and an increase of the electron density (panel f).

The maximum intensity of the radio emission (and the closest to f_{ce}) is observed between 07:37:25 and 07:37:30 (panel b), where a loss cone is observed in the up-going electron distribution function (panel e), i.e. the electron distribution function at low pitch angle from 0° to $\sim 25°$ is much lower than at higher pitch angle (50°–60°).

3 The Cyclotron Maser Instability: determination of the emission parameters

In this Section, we review the main details of the CMI that will be used in this study. For more details, please refer to Wu and Lee (1979); Wu (1985); Le Queau et al. (1984b, 1984a); Pritchett (1986a); Treumann (2006); Louarn et al. (2017).

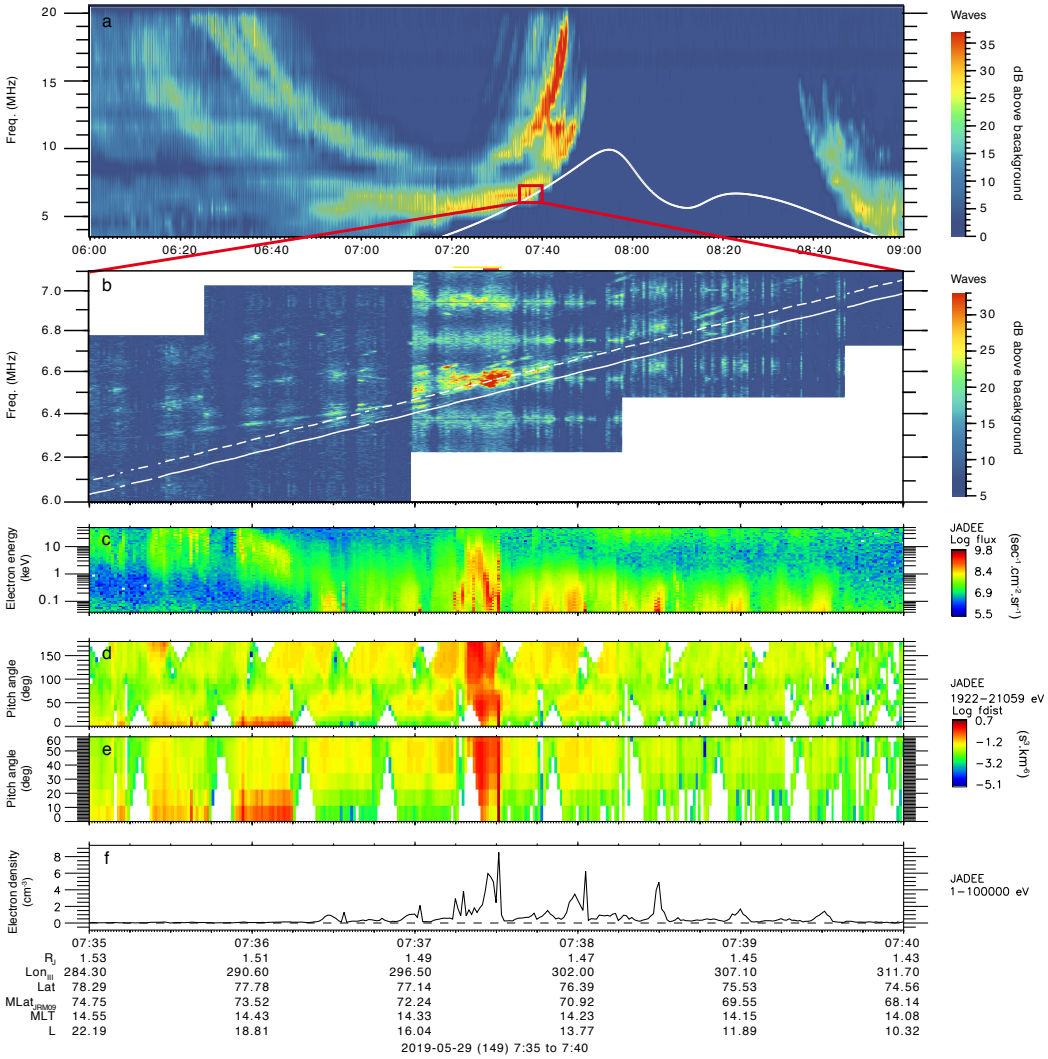

Figure 1. Juno measurements around the Ganymede's tail footprint encounter (from 7:37:14 to 07:37:32, Szalay et al., 2020a).

Panels (a,b) display Juno/Waves data (a) in low-resolution mode and (b) in high-resolution mode. The solid-white lines represent the electron cyclotron frequency derived from the magnetic field measurements of Juno/MAG, and the dashed-white line is $1.01 \times f_{ce}$.

Panels (c-f) display Juno/JADE-E measurements: (c) the electron differential energy flux; (d) the electron distribution function for energy in range [2-21] keV at all pitch angles; (e) same as panel (d) but only for pitch angles [0°-60°] corresponding to up-going electrons; (f) the partial electron density calculated from JADE-E 3D moments.

The CMI is a wave-particle instability for which the resonance is reached when the Doppler-shifted angular frequency of the wave in the frame of the electron ($\omega - k_{||} v_{r_{||}}$) is equal to the relativistic gyration frequency of resonant electron ($\omega_{ce}\Gamma_r^{-1}$). Thus, the resonance condition can be written as:

$$\omega = 2\pi f = \omega_{ce}\Gamma_r^{-1} + k_{||} v_{r_{||}}, \tag{1}$$

where the $_{||}$ index describes the component parallel to the magnetic field line, k the wave vector, v_r the resonant electron velocity and $\Gamma_r^{-1} = \sqrt{1 - v_r^2/c^2}$ the Lorentz factor associated with the motion of resonant electrons.

In the weakly relativistic case ($v_r << c$) the above resonance condition can be rewritten as the equation for a resonant circle in the $[v_\perp, v_{||}]$ velocity space:

$$v_{r\perp}^2 + (v_{r||} - \frac{k_{||} c^2}{\omega_{ce}})^2 = c^2 \left(\frac{k_{||}^2 c^2}{\omega_{ce}^2} + 2(1 - \frac{\omega}{\omega_{ce}}) \right). \tag{2}$$

The resonance circle center v_0 (located on the $v_{||}$ axis) and its radius R are thus defined as:

$$v_0 = \frac{k_{||} c^2}{\omega_{ce}} = \frac{\omega}{\omega_{ce}} c N cos\theta, \tag{3}$$

where θ is the propagation angle of the emission with respect to the local magnetic field lines ($kcos\theta = \vec{k} \cdot \vec{b} = k_{||}$) and $N = ck/\omega$ is the refractive index value;

$$R = c \left(\frac{k_{||}^2 c^2}{\omega_{ce}^2} + 2(1 - \frac{\omega}{\omega_{ce}}) \right)^{1/2} = c \left(\frac{v_0^2}{c^2} - 2\Delta\omega \right)^{1/2}, \tag{4}$$

where

$$\Delta\omega = (\omega - \omega_{ce})/\omega_{ce} \tag{5}$$

is the frequency shift.

It is then necessary to determine the optimal electron population that will lead to the amplification of the wave and the production of the emission, which is done by calculating and maximizing the growth rate along different resonance circles. The simplified version used by Louarn et al. (2017) is perfectly adapted to the amplification of X-mode waves propagating at frequencies close to $f_{\rm ce}$, for $N \simeq 1$, in a moderately energetic ($E << m_{\rm e}c^2 = 511$ keV) and low-density ($f_{\rm pe}/f_{\rm ce} << 1$) plasma. Since the electron energy is equal to a few 0.1 keV to a few keV (see Fig. 1c) and the electron density is equal to a few particles per cm^{-3} (see Fig. 1f), we can use the simplified formula of Louarn et al. (2017) to calculate the normalized growth rate of the instability along resonant circles in the normalized velocity space $[\beta_{||}, \beta_\perp]$, with $\beta = v/c$, expressed as:

$$\frac{\gamma}{\omega_{\rm ce}} \simeq 2\pi^2 \Delta\omega^2 \int_0^\pi d\phi \; b^2 \; sin^2(\phi) \frac{\partial}{\partial \beta_\perp} f_b(\beta_0 + b \; cos(\phi), b \; sin(\phi)), \tag{6}$$

where $\beta_0 = v_0/c$ is the center (see Eq. 3) and $b = R/c$ the radius (see Eq. 4) of the resonant circle, $\Delta\omega$ the frequency shift (see Eq. 5) and f the normalized electron distribution function ($\int f dv^3 = 1$). In practice, the factor to normalize the distribution function is $c^3 10^{-18}/n_e$, where n_e is the density (in cm^{-3}). Here $n_e \simeq 1$ cm^{-3} at 07:36:40, and $n_e \simeq 6$ cm^{-3} at 07:37:26 and 07:37:28, and $n_e \simeq 2$ cm^{-3} at 07:37:43 (see Fig. 1f), which is probably slightly overestimated (Allegrini et al., 2020), leading to underestimated growth rate.

Eq. 6 means that the growth rate is obtained by integrating $\partial f/\partial\beta_\perp$ along a resonant circle in the normalized velocity space $[\beta_{||}, \beta_\perp]$ defined by its center β_0, radius b, and angle ϕ.

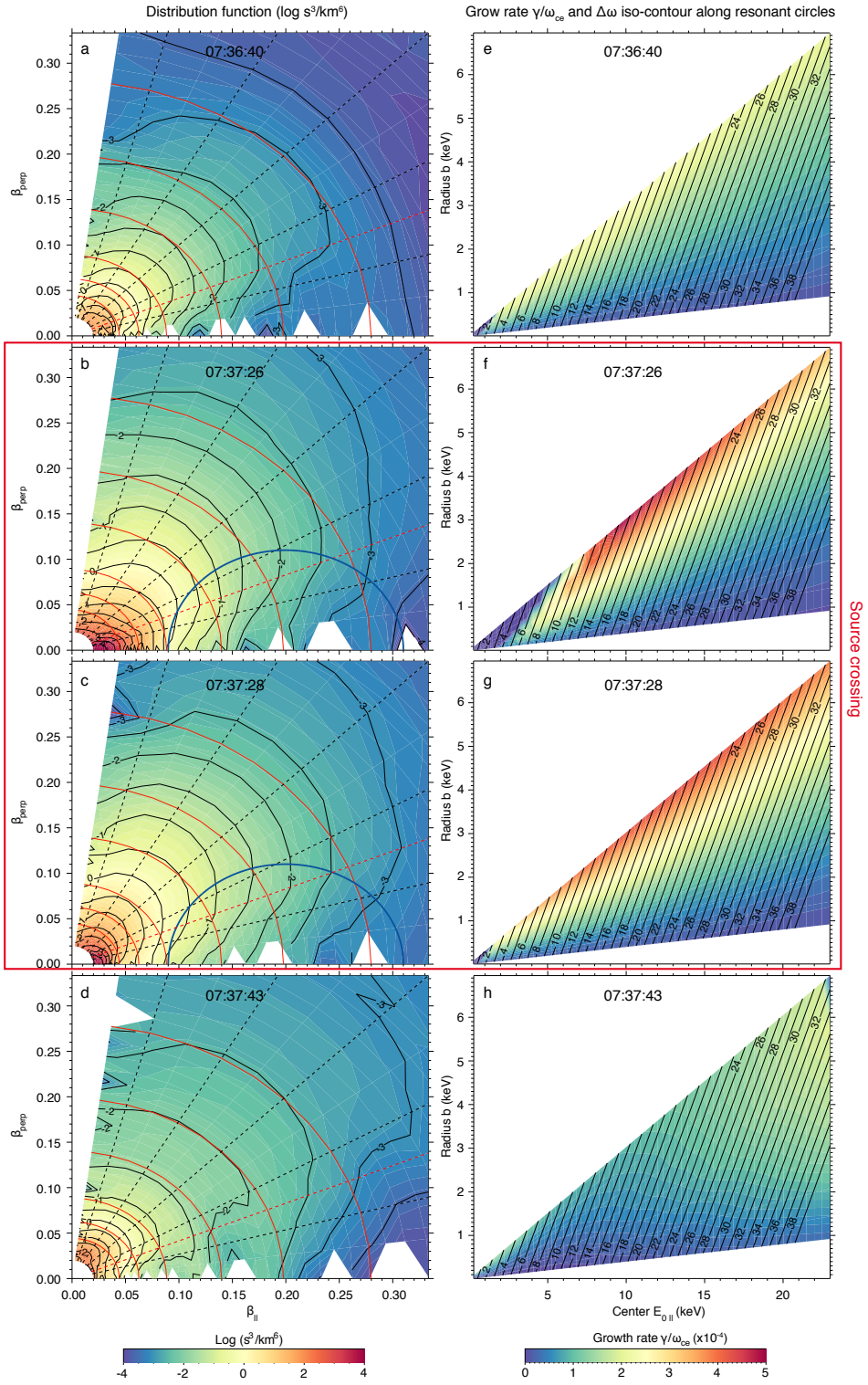

Figure 2. Panels (a-d): upgoing electron distribution function in the normalized velocity space $[\beta_{||},\beta_{\perp}]$ measured by JADE-E on 2019-05-29 at (a) 07:36:40, (b) 07:37:26, (c) 07:37:28 and (d) 07:37:43. The isocontours are shown using a logarithmic scale in units of s^3/km^6. The red circular arcs correspond to iso-energies of 0.5, 1, 2, 5, 10 and 20 keV and the radial black-dashed lines to pitch angles of 15°, 30°, 45°, 60° and 75°. The radial red-dashed line at pitch angle 22.5° displays the lower limit of the loss cone. An example of a resonant circle is displayed in blue in panels (b,c).

Panels (e-h): normalized growth rate γ/ω_{ce} estimates for different resonant circles at different center $E_{0||}$ and radius b, at (e) 07:36:40, (f) 07:37:26, (g) 07:37:28 and (h) 07:37:43. The over-plotted black lines represent the isocontours of $\Delta\omega = (\omega - \omega_{ce})/\omega_{ce} \times 10^3$.

3.1 Electron distribution function

Figures 2a-d display the distribution functions of upgoing electrons (pitch angle from 0° to 82.5°) measured by Juno/JADE-E at (a) 07:36:40, (b) 07:37:26, (c) 07:37:28 and (d) 07:37:43. Fig. 2b,c correspond to the period of maximum increasing decametric flux seen in Fig. 1b, while Fig. 2a,d correspond to time where Juno is outside the Ganymede flux tube. The colors correspond to different electron distribution function iso-contours, using a logarithmic scale in units of s^3/km^6. A loss cone in each distribution is clearly visible for pitch angle at least lower than 22.5° (dashed-red line), when iso-contours are not following the iso-energy curves (red-circles). Note that at high pitch angle ($> 75°$), the iso-contours do not follow the iso-energy circles, which is due to spacecraft shadowing (Allegrini et al., 2017, 2020).

Compared to 07:36:40 and 07:37:43, the distribution functions at 07:37:26 and 07:37:28 show larger phase space density at every energy (the isocontours are enlarged), which corresponds to a denser, hotter and more energized plasma.

3.2 Estimation of growth rate and emission characteristics

From Fig. 2a-d and Eq. 6, we can calculate the normalized growth rate along different resonant circles to determine the optimal electron population. An example of a resonant circle is displayed Fig. 2b,c in blue, with a center $\beta_{0||} \simeq 0.20$ (i.e. ~ 10 keV) and a radius $b = 0.11$ (i.e. ~ 3 keV).

Figures 2e-h display the estimated normalized growth rate γ/ω_{ce} along resonant circles, calculated for different center $E_0 = \beta_0^2 * 255.5$ and different radius b (taken from $0.2–0.6 \times \beta_0$). The overplotted black lines represent the $\Delta\omega$ value at each point of the resonant circles, calculated as $\Delta\omega = (\beta_0^2 - b^2)/2$ (see eq. 4). Maximal growth rates are obtained during the source crossing (Fig. 2f,g), with values above 3×10^{-4} (orange to red regions), sufficient for the production of radio emission.

Pritchett (1986b) performed numerical simulations of the weakly relativistic loss-cone maser instability, and determined (i) that the more the emission angle θ turns away from the perpendicular direction the weaker the emission is, and (ii) that at $\theta < 80°$ the emission intensity drastically drops to the background noise level (and reaches it at $\theta = 70°$). This was also observed by Louis, Lamy, Zarka, Cecconi, Imai, et al. (2017), for the simulated Io-decametric-induced emission not visible for $\theta < 75° \pm 5°$. Looking at the Juno/Waves high-resolution data during the source crossing, we can constrain this limit even further, since during the source crossing (between 07:37:25 and 07:37:30), no emission is observed above $f_{ce} \times 1.021$ (i.e. $\Delta\omega = 0.021$). From these considerations, we can infer that large amplifications are obtained for energies in the range $\sim$[6-15] keV at 07:37:26 and $\sim$[4-15] keV at 07:37:28, at a frequency shift $\Delta\omega = 8\text{-}21 \times 10^{-3}$ and $5\text{-}21 \times 10^{-3}$ respectively.

Using the equations 3-5, assuming a refractive index N very close to 1 due to the very low-density plasma ($f_{pe} << f_{ce}$), we can derive the propagation angle θ:

$$\theta = acos\left(\beta_0/(1 + \Delta\omega)\right). \tag{7}$$

We can then determine that the observed emission propagates at an angle θ varying from $\sim 81°$ to $\sim 76°$ (07:37:26) and from $\sim 83°$ to $\sim 76°$ (07:37:28).

The measured B amplitude at 07:37:26 (07:37:28) gives an electron plasma frequency $f_{ce} \simeq 6484$ kHz ($\simeq 6490$ kHz). Thus, $\Delta\omega \simeq 8-21 \times 10^{-3}$ ($5\text{-}21 \times 10^{-3}$) is equivalent to an emission frequency at $\sim 6535-6620$ kHz ($\sim 6522-6626$ kHz), which explains why we observe emission closer to f_{ce} at 07:37:28 in the Juno/Waves data (see Fig. 1b).

4 Conclusion and Discussion

In conclusion, we analyzed the first example of in-situ particle measurements of a Ganymede-induced radio emission, during the Ganymede's tail flux tube crossing (Szalay et al., 2020a) connected to FUV emission. Looking at the distribution functions before,during and after the source crossing, we showed that the loss cone-driven CMI can explain the generation of decametric radio emission. The electron population involved in this emission has an energy of 4−15 keV, with a wave propagation angle θ varying from 83° to 76°, at a frequency shift $\Delta\omega = 5 - 21 \times 10^{-3}$. Furthermore, the electron distribution functions show that a denser, hotter and more energized plasma (observed only during the source crossing, see Fig. 2) is necessary to allow the CMI to occur.

Szalay et al. (2020a) showed that in this present case, Ganymede's footprint tail is sustained by Alfvnic acceleration processes. Thus, as suggested by Louarn et al. (2018), all the radio emissions seem to be triggered by Alfvnic acceleration (as at Earth, Su et al., 2007). Furthermore, we now have direct proof that radio emission is associated with a Ganymede down-tail FUV emission, likely one of the reflected Alfvn waves originally generated at Ganymede (as is the case for Io).

Looking at the data of Fig. 1, Juno spent at least $\sim 4-6$ sec crossing the source of Ganymede-induced radio emission. Juno's velocity was ~ 50 km/s^{-1} during the source crossing, thus we can determine a source size of at least $\sim 250 \pm 50$ km. Taking a radio wave propagating at the light speed, the wave spent 0.67−1 ms inside the source. Since at 07:37:26 $f_{ce} = 6484$ kHz and $\gamma/\omega_{ce} = 3-4\times10^{-4}$, we can determine that the growth rate γ is equal to $\simeq 10 - 20 \times 10^3$ s^{-1}. At light speed, propagation of $\sim 150 -$ 300 km is then sufficient to amplify the waves by a factor e^{10}, which is fully compatible with the measured size of the source and the observed intensity of the emission which peaks at ~ 45 dB above the background at 07:37:28.

The loss-cone-driven CMI then seems to be a common way to amplify waves and produce radio emissions, sustained by an Alfvnic acceleration process in the case of auroral radio emissions (Louarn et al., 2017, 2018) as in the case of moon-induced radio emissions (present study). The next step should be to study the more numerous radio source crossings of Io's tail (Szalay et al., 2018; Louis et al., 2019; Szalay et al., 2020b), in order to explain (i) how radio emission can be produced 10s of degrees away from the main Alfvn Wing spot, (ii) why these radio emissions are not observed from a distant point of view and (iii) how the electron distribution function and the radio emission intensity evolve with distance from the Main Alfvn Wing spot.

Acknowledgments

The authors thank the Juno mission team, especially the staff of the Waves and JADE instruments. The Juno data used in this manuscript are reachable from the Planetary Data System at https://pds-ppi.igpp.ucla.edu/mission/JUNO in the JAD > JUNO JADE CALIBRATED SCIENCE DATA > DATA > 2019 > 2019149 > ELECTRONS tab for JADE-E data, in the WAV > JUNO WAVES BURST STANDARD SCIENCE PRODUCTS > DATA > WAVES_BURST > 2019122_ORBIT_20 > WAV_2019149T071635_NBS_REC_V01 tab for Waves burst mode data and in the WAV > JUNO WAVES SURVEY STANDARD SCIENCE PRODUCTS > DATA > WAVES_SURVEY > 2019122_ORBIT_20 > WAV_2019149T000000_E_V01 tab for Waves survey data. C. K. L. acknowledges funding support from the CNES, and thanks E. Penou, for the help with the particle analysis through the CLWeb software. The research at the University of Iowa is supported by NASA through Contract 699041X with the Southwest Research Institute.

References

Allegrini, F., Bagenal, F., Bolton, S., Connerney, J., Clark, G., Ebert, R. W., ...

Zink, J. L. (2017, July). Electron beams and loss cones in the auroral regions of Jupiter. *Geophysical Research Letters*, *44*(14), 7131-7139. doi: 10.1002/2017GL073180

Allegrini, F., Mauk, B., Clark, G., Gladstone, G. R., Hue, V., Kurth, W. S., ... Wilson, R. J. (2020, April). Energy Flux and Characteristic Energy of Electrons Over Jupiter's Main Auroral Emission. *Journal of Geophysical Research (Space Physics)*, *125*(4), e27693. doi: 10.1029/2019JA027693

Bagenal, F., Adriani, A., Allegrini, F., Bolton, S. J., Bonfond, B., Bunce, E. J., ... Zarka, P. (2017, November). Magnetospheric Science Objectives of the Juno Mission. *Space Science Reviews*, *213*, 219-287. doi: 10.1007/s11214-014-0036-8

Bigg, E. K. (1964, September). Influence of the Satellite Io on Jupiter's Decametric Emission. *Nature*, *203*, 1008-1010. doi: 10.1038/2031008a0

Clarke, J. T. (1998). Hubble space telescope imaging of jupiter's uv aurora during the galileo orbiter mission. *Journal of Geophysical Research: Planets*, *103*(E9), 20217-20236. doi: 10.1029/98JE01130

Clarke, J. T., Ajello, J., Ballester, G., Ben Jaffel, L., Connerney, J., Gérard, J.-C., ... Waite, J. H. (2002, February). Ultraviolet emissions from the magnetic footprints of Io, Ganymede and Europa on Jupiter. *Nature*, *415*, 997-1000.

Connerney, J. E. P., Benn, M., Bjarno, J. B., Denver, T., Espley, J., Jorgensen, J. L., ... Smith, E. J. (2017, November). The Juno Magnetic Field Investigation. *Space Science Reviews*, *213*, 39-138. doi: 10.1007/s11214-017-0334-z

Hess, S. L. G., Delamere, P., Dols, V., Bonfond, B., & Swift, D. (2010, June). Power transmission and particle acceleration along the Io flux tube. *Journal of Geophysical Research (Space Physics)*, *115*, A06205. doi: 10.1029/2009JA014928

Imai, M., Greathouse, T. K., Kurth, W. S., Gladstone, G. R., Louis, C. K., Zarka, P., ... Connerney, J. E. P. (2019, Jan). Probing Jovian Broadband Kilometric Radio Sources Tied to the Ultraviolet Main Auroral Oval With Juno. *Geophysical Research Letters*, *46*(2), 571-579. doi: 10.1029/2018GL081227

Imai, M., Kurth, W. S., Hospodarsky, G. B., Bolton, S. J., Connerney, J. E. P., & Levin, S. M. (2017, July). Direction-finding measurements of Jovian low-frequency radio components by Juno near Perijove 1. *Geophysical Research Letters*, *44*, 6508-6516. doi: 10.1002/2017GL072850

Kurth, W. S., Hospodarsky, G. B., Kirchner, D. L., Mokrzycki, B. T., Averkamp, T. F., Robison, W. T., ... Zarka, P. (2017, November). The Juno Waves Investigation. *Space Science Reviews*, *213*, 347-392. doi: 10.1007/s11214-017-0396-y

Le Queau, D., Pellat, R., & Roux, A. (1984a, January). Direct generation of the auroral kilometric radiation by the maser synchrotron instability: An analytical approach. *Physics of Fluids*, *27*(1), 247-265. doi: 10.1063/1.864520

Le Queau, D., Pellat, R., & Roux, A. (1984b, May). Direct generation of the auroral kilometric radiation by the maser synchrotron instability: Physical mechanism and parametric study. *Journal of Geophysical Research*, *89*(A5), 2831-2841. doi: 10.1029/JA089iA05p02831

Louarn, P., Allegrini, F., McComas, D. J., Valek, P. W., Kurth, W. S., André, N., ... Zink, J. L. (2017, May). Generation of the Jovian hectometric radiation: First lessons from Juno. *Geophysical Research Letters*, *44*, 4439-4446. doi: 10.1002/2017GL072923

Louarn, P., Allegrini, F., McComas, D. J., Valek, P. W., Kurth, W. S., André, N., ... Wilson, R. J. (2018, September). Observation of Electron Conics by Juno: Implications for Radio Generation and Acceleration Processes. *Geophysical Research Letters*, *45*(18), 9408-9416. doi: 10.1029/2018GL078973

Louis, C. K., Lamy, L., Zarka, P., Cecconi, B., & Hess, S. L. G. (2017, September). Detection of Jupiter decametric emissions controlled by Europa and Ganymede with Voyager/PRA and Cassini/RPWS. *Journal of Geophysical Research*

(Space Physics), *122*, 9228-9247. doi: 10.1002/2016JA023779

Louis, C. K., Lamy, L., Zarka, P., Cecconi, B., Imai, M., Kurth, W. S., ... Levin, S. M. (2017, September). Io-Jupiter decametric arcs observed by Juno/Waves compared to ExPRES simulations. *Geophysical Research Letters*, *44*, 9225-9232. doi: 10.1002/2017GL073036

Louis, C. K., Prangé, R., Lamy, L., Zarka, P., Imai, M., Kurth, W. S., & Connerney, J. E. P. (2019, November). Jovian Auroral Radio Sources Detected In Situ by Juno/Waves: Comparisons With Model Auroral Ovals and Simultaneous HST FUV Images. *Geophysical Research Letters*, *46*(21), 11,606-11,614. doi: 10.1029/2019GL084799

McComas, D. J., Alexander, N., Allegrini, F., Bagenal, F., Beebe, C., Clark, G., ... White, D. (2017, November). The Jovian Auroral Distributions Experiment (JADE) on the Juno Mission to Jupiter. *Space Science Reviews*, *213*, 547-643. doi: 10.1007/s11214-013-9990-9

Prangé, R., Rego, D., Southwood, D., Zarka, P., Miller, S., & Ip, W. (1996, January). Rapid energy dissipation and variability of the lo-Jupiter electrodynamic circuit. *Nature*, *379*, 323-325. doi: 10.1038/379323a0

Pritchett, P. L. (1986a, December). Cyclotron maser radiation from a source structure localized perpendicular to the ambient magnetic field. *Journal of Geophysical Research*, *91*(A12), 13569-13582. doi: 10.1029/JA091iA12p13569

Pritchett, P. L. (1986b, September). Electron-cyclotron maser instability in relativistic plasmas. *Physics of Fluids*, *29*(9), 2919-2930. doi: 10.1063/1.865492

Su, Y.-J., Ergun, R. E., Jones, S. T., Strangeway, R. J., Chaston, C. C., Parker, S. E., & Horwitz, J. L. (2007, June). Generation of short-burst radiation through Alfvénic acceleration of auroral electrons. *Journal of Geophysical Research (Space Physics)*, *112*(A6), A06209. doi: 10.1029/2006JA012131

Szalay, J. R., Allegrini, F., Bagenal, F., Bolton, S. J., Bonfond, B., Clark, G., ... Wilson, R. J. (2020a, February). Alfvénic Acceleration Sustains Ganymede's Footprint Tail Aurora. *Geophysical Research Letters*, *47*(3), e86527. doi: 10.1029/2019GL086527

Szalay, J. R., Allegrini, F., Bagenal, F., Bolton, S. J., Bonfond, B., Clark, G., ... Wilson, R. J. (2020b). A new framework to explain changes in Io's footprint tail electron fluxes, submitted. *Geophysical Research Letters*.

Szalay, J. R., Bonfond, B., Allegrini, F., Bagenal, F., Bolton, S., Clark, G., ... Wilson, R. J. (2018). In situ observations connected to the io footprint tail aurora. *Journal of Geophysical Research: Planets*, *123*(11), 3061-3077. doi: 10.1029/2018JE005752

Treumann, R. A. (2006, August). The electron-cyclotron maser for astrophysical application. *Astronomy & Astrophysicsr*, *13*, 229-315. doi: 10.1007/s00159-006-0001-y

Wu, C. S. (1985, August). Kinetic cyclotron and synchrotron maser instabilities - Radio emission processes by direct amplification of radiation. *Space Science Reviews*, *41*, 215-298. doi: 10.1007/BF00190653

Wu, C. S., & Lee, L. C. (1979, June). A theory of the terrestrial kilometric radiation. *Astrophysical Journal*, *230*, 621-626. doi: 10.1086/157120

Zarka, P., Marques, M. S., Louis, C., Ryabov, V. B., Lamy, L., Echer, E., & Cecconi, B. (2017, January). Radio emission from satellite-Jupiter interactions (especially Ganymede). In G. Fischer, G. Mann, M. Panchenko, & P. Zarka (Eds.), *Planetary radio emissions viii* (p. 45-58). doi: 10.1553/PRE8s45

Zarka, P., Marques, M. S., Louis, C., Ryabov, V. B., Lamy, L., Echer, E., & Cecconi, B. (2018, October). Jupiter radio emission induced by Ganymede and consequences for the radio detection of exoplanets. *Astronomy & Astrophysics*, *618*, A84. doi: 10.1051/0004-6361/201833586

Figure1.

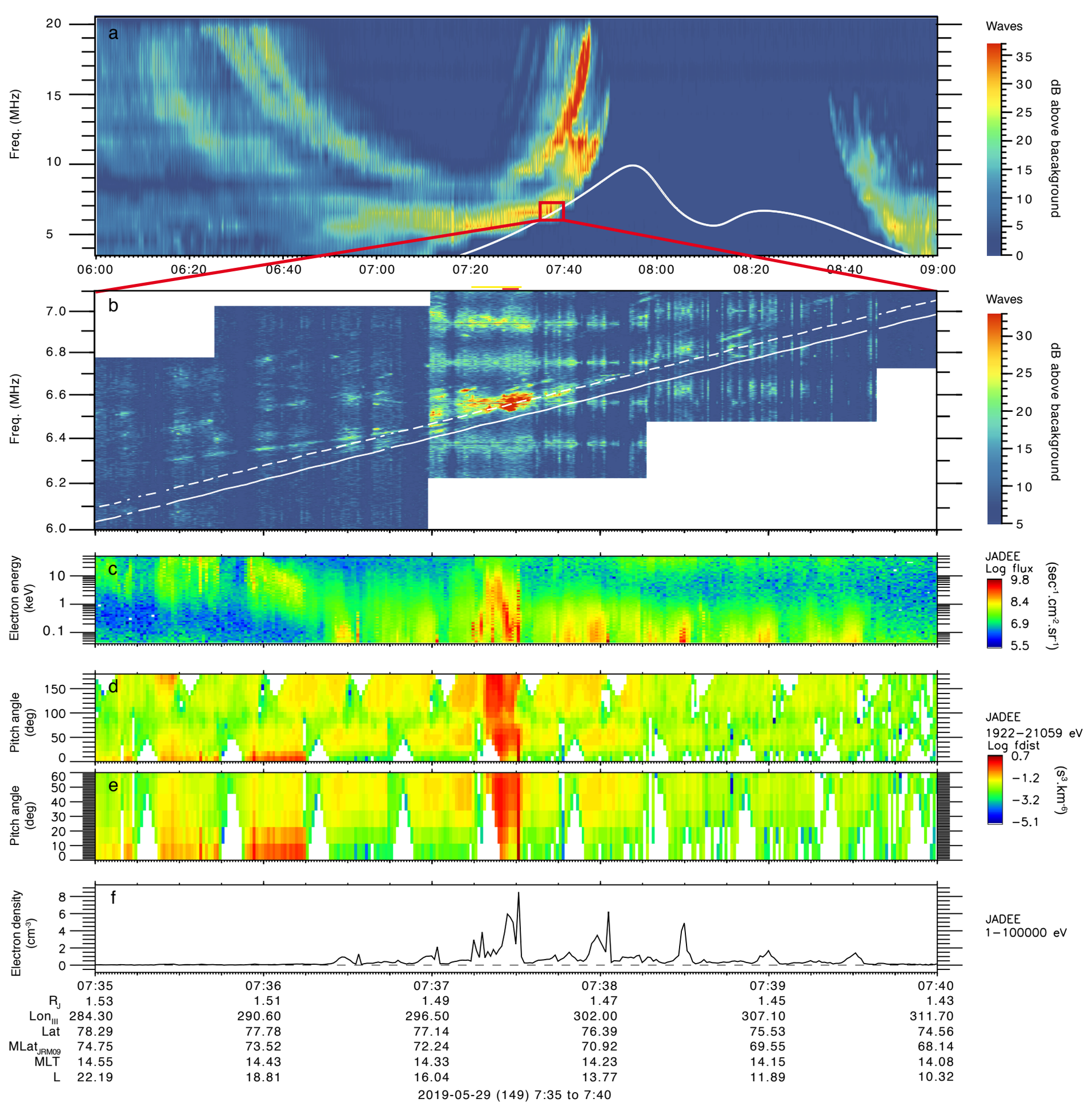
a
Freq. (MHz)
20
15
10
5
06:00
06:20
06:40
07:00
07:20
07:40
08:00
08:20
08:40
09:00
Waves
dB above bacakground
35
30
25
20
15
10
5
0
b
Freq. (MHz)
7.0
6.8
6.6
6.4
6.2
6.0
Waves
dB above bacakground
30
25
20
15
10
5
c
Electron energy (keV)
10
1
0.1
JADEE
Log flux
(sec-1.cm-2.sr-1)
9.8
8.4
6.9
5.5
d
Pitch angle (deg)
150
100
50
0
JADEE
1922−21059 eV
Log fdist
(s3.km-6)
0.7
−1.2
−3.2
−5.1
e
Pitch angle (deg)
60
50
40
30
20
10
0
f
Electron density (cm-3)
8
6
4
2
0
JADEE
1−100000 eV
07:35
07:36
07:37
07:38
07:39
07:40
RJ 1.53 1.51 1.49 1.47 1.45 1.43
LonIII 284.30 290.60 296.50 302.00 307.10 311.70
Lat 78.29 77.78 77.14 76.39 75.53 74.56
MLatJRM09 74.75 73.52 72.24 70.92 69.55 68.14
MLT 14.55 14.43 14.33 14.23 14.15 14.08
L 22.19 18.81 16.04 13.77 11.89 10.32
2019-05-29 (149) 7:35 to 7:40

Figure2.

Distribution function (log s^3/km^6)

Grow rate γ/ω_{ce} and $\Delta\omega$ iso-contour along resonant circles

a 07:36:40

b 07:37:26

c 07:37:28

d 07:37:43

e 07:36:40

f 07:37:26

g 07:37:28

h 07:37:43

β_{perp}

$\beta_{||}$

Radius b (keV)

Center $E_{0||}$ (keV)

Log (s^3/km^6)

Growth rate γ/ω_{ce} ($x10^{-4}$)

Source crossing